SCIENCE CHINA
Physics, Mechanics & Astronomy

•Article•

September 2020 Vol. 63 No. 9: 297511
https://doi.org/10.1007/s11433-019-1525-6

Structure and strain tunings of topological anomalous Hall effect in cubic noncollinear antiferromagnet Mn_3Pt epitaxial films

Ning An[†], Meng Tang[†], Shuai Hu, HuangLin Yang, WeiJia Fan, ShiMing Zhou, and XuePeng Qiu[*]

Shanghai Key Laboratory of Special Artificial Microstructure Materials and Technology, School of Physics Science and Engineering, Tongji University, Shanghai 200092, China

Received December 19, 2019; accepted February 11, 2020; published online May 13, 2020

Antiferromagnets (AFMs) with chiral noncollinear spin structure have attracted great attention in recent years. However, the existing research has mainly focused on hexagonal chiral AFMs, such as Mn_3Sn, Mn_3Ga, Mn_3Ge with low crystalline symmetry. Here, we present our systematical study for the face-centered cubic noncollinear antiferromagnetic Mn_3Pt. By varying the alloy composition (x), we have successfully fabricated antiferromagnetic $Mn_{1-x}Pt_x$ epitaxial films on MgO substrates and have observed a crystalline structure transition from $L1_0$ MnPt to $L1_2$ Mn_3Pt. The Mn_3Pt exhibits a large anomalous Hall effect, which is in the same order of magnitude as those of ferromagnetic materials. Moreover, a large thickness-evolved strain effect is revealed in Mn_3Pt films by X-ray diffraction (XRD) analysis based on the Scherrer method. Our work explores Mn_3Pt as a promising candidate for topological antiferromagnetic spintronics.

anomalous Hall effect, noncollinear antiferromagnet, strain effect, $L1_0$ and $L1_2$ alloys

PACS number(s): 75.50.Ee, 75.47.-m, 75.70.-i

Citation: N. An, M. Tang, S. Hu, H. L. Yang, W. J. Fan, S. M. Zhou, and X. P. Qiu, Structure and strain tunings of topological anomalous Hall effect in cubic noncollinear antiferromagnet Mn_3Pt epitaxial films, Sci. China-Phys. Mech. Astron. **63**, 297511 (2020), https://doi.org/10.1007/s11433-019-1525-6

1 Introduction

Anomalous Hall effect (AHE) was discovered in ferromagnets by Edwin Hall in 1881 [1] and has attracted immense interest over the past several decades [2-7]. Empirically, the AHE has been generally correlated with the spontaneous magnetization of a material; thus, the studies of the AHE have mostly focused on ferromagnetic materials, such as Ni, Fe, Co, and their compounds. Until recently, researchers have explored AHE in antiferromagnets (AFMs) with almost zero magnetization but instead, with robust topological spin structure [8-14]. Such topological AHE quickly becomes the forefront of the emerging research field of topological spintronics [15-18]. AHE in AFMs was theoretically predicted by Chen et al. [8] that a broken mirror symmetry combined with spin-orbit coupling could lead to nontrivial AHE in an AFM such as Mn_3Ir, which is closely related to the topological properties of Bloch bands emphasized by Liu et al. [13]. Therefore, this phenomenon is intrinsically a topological manifestation of magnetism. After the first theoretical prediction, a surprisingly large AHE was experimentally reported in the antiferromagnetic Mn_3Sn bulk crystal for the first time [9] and has stimulated worldwide research interest in the AFMs with topological spin structures manifested by the noncollinear spin alignment between neighbor electrons. Not only the large AHE [9,10,13,19] but many other interesting physical phenomena such as spin Hall

[*]Corresponding author (email: xpqiu@tongji.edu.cn)
[†]These authors contributed equally to this work.

effect (SHE) [12,20], spin-polarized current [21], anomalous Nernst effect (ANE) [22-24], spin Nernst effect (SNE) [25], and magneto-optical Kerr effect (MOKE) [26,27] have also been found in noncollinear antiferromagnetic materials.

The noncollinear AFMs can be classified into two categories by the crystalline structure. The first one is Mn_3X (X = Sn, Ge or Ga) with hexagonal lattice structure with space group $P6_3/mmc$ of Ni_3Sn-type structure. The second one is Mn_3Y (Y = Ir or Pt) of $L1_2$ (Cu_3Au) cubic crystal lattice with space group $Pm\bar{3}m$. The reduced crystalline symmetry in hexagonal Mn_3X compared to the cubic Mn_3Y allows easier saturation within the magnetic fields available in the laboratory; thus, the study of cubic Mn_3Y antiferromagnetic material has remained limited. From the few studies, it has been shown that Mn_3Pt has two antiferromagnetic phases [13,28,29]. One phase existing below the phase transition temperature (360 K) is called D phase for which spin moments of three Mn atoms order in a triangular arrangement in (111) crystal plane, and a large AHE emerges. The other phase is called F phase in which at high temperatures, the spin moments are in collinear arrangement; thus, AHE disappears [13,28,30,31]. Liu et al. [13] have reported the effective toggling between these two phases, and in turn, the manipulation of the AHE of Mn_3Pt through an electric field, showing the prospect of utilizing antiferromagnetic Mn_3Pt for information storage. However, prior studies on Mn_3Pt alloy, especially the phase diagram, crystalline structure, as well as the magnetic property of $Mn_{1-x}Pt_x$, require further work. Moreover, the examination of strain effect still lacks for Mn_3Pt, although the epitaxial growth of Mn_3Y alloy and the emergence of Mn_3Pt D phase require careful lattice and strain engineering.

In this work, we report the fabrication of high-quality epitaxial $L1_2$ Mn_3Pt ordered alloy films on MgO (001) substrates. Studies of the thickness-dependent structural, electrical, and magnetic properties of the Mn_3Pt films are performed. We first show the influence of the composition of $Mn_{1-x}Pt_x$ films on their structural properties and AHE, and determination of the optimal composition for fabricating high-quality $L1_2$ Mn_3Pt films. Then, by changing film thickness, we demonstrate a large strain manipulation of Mn_3Pt films [32-34]. Finally, we discuss the influence of film strain on the magnetic properties of $L1_2$ Mn_3Pt films.

2 Experiments

To study the optimal condition for fabricating Mn_3Pt films by magnetron co-sputtering, the annealing temperature and composition of $Mn_{1-x}Pt_x$ were systematically changed. Previous studies have reported that ordered Mn_3Pt, MnPt, and $MnPt_3$ phases are stable in 16%-29% Pt, 33%-60% Pt, and 63%-83% Pt concentration ranges at room temperature, respectively [31]. By calibrating the growth rates of the Mn layer and Pt layer at different sputtering powers, we estimated that sputtering powers for obtaining a stoichiometric Mn_3Pt film are 56 W for sputtering Mn and 30 W for sputtering Pt. We fixed the Pt sputtering power at 30 W and varied the Mn sputtering power to tune the composition of $Mn_{1-x}Pt_x$. Before depositing each $Mn_{1-x}Pt_x$, MgO (001) was pre-annealed for 0.5 h at 730°C to obtain smooth and clean substrates. The deposition of $Mn_{1-x}Pt_x$ was performed at 600°C. Ar gas pressure was 2.6 mTorr. The deposition rate of $Mn_{1-x}Pt_x$ film was calibrated to be 0.4 Å s^{-1}. After deposition, $Mn_{1-x}Pt_x$ films with variable thickness were annealed at 600°C for 3 h to achieve better crystal quality. After the $Mn_{1-x}Pt_x$ films were naturally cooled to room temperature, 3 nm SiN were subsequently deposited to serve as insulating protection layers. The crystal structure of $Mn_{1-x}Pt_x$ films was characterized by X-ray diffraction (XRD) by a Bruker D8 diffractometer with a five-axis configuration and Cu Kα (λ = 0.15419 nm). The film thickness and surface roughness were characterized by X-ray reflectivity (XRR). The epitaxial growth of the films was proven by X-ray pole figures. The alloy composition was measured by energy-dispersive X-ray spectroscopy (EDS). The longitudinal resistivity (ρ_{xx}) and transverse resistivity (ρ_{xy}) were measured in the temperature region from 10 to 395 K in the standard Hall bar devices made from the $Mn_{1-x}Pt_x$ films. The anomalous Hall resistivity ρ_{AHE} was obtained by extrapolating ρ_{xy} data from a high magnetic field to zero field in the AHE loops.

3 Results and discussion

Mn_3Pt is a cubic AFM that exhibits noncollinear ordering of Mn magnetic moments at room temperature and its Néel temperature T_N ~475 K [13,30]. The magnetic moments on Mn atoms establish normal triangular magnetic order structures, as shown in Figure 1(a). The angle of the magnetic moments of adjacent Mn atoms is 120°. Figure 1(b) and (c) show the typical XRD patterns for the crystal structure of a 25-nm Mn_3Pt film fabricated with co-sputtering powers 56 W (Mn) and 30 W (Pt). The out-of-plane XRD θ-2θ scans at different planes indicate that the Mn_3Pt film on MgO is a (001) oriented single crystal, as shown in Figure 1(b). The 360° ϕ scans around the (111) peaks of Mn_3Pt and MgO confirm the epitaxial growth in Figure 1(c).

To study the optimal growth conditions for growing Mn_3Pt, namely the best power ratio of Mn sputtering power to Pt sputtering power, we kept the Pt sputtering power (radio frequency, RF) at 30 W while changing the sputtering power of Mn (direct current, DC) from 32 to 64 W with an 8 W step. The EDS measurements show that the ratio of Mn to Pt in the film is closest to 3∶1 when the Mn sputtering power is 56 W. The XRR analysis shows these films have a thickness

in the range of 10-20 nm. The XRD results indicate that when the Mn sputtering power is greater than 48 W, $L1_2$ Mn_3Pt is obtained, and when it is less than 48 W, $L1_0$ MnPt is formed. Figure 2(a) shows the XRD spectra of $Mn_{1-x}Pt_x$ films at different Mn sputtering powers. As the growth power of Mn is increased, the composition of $Mn_{1-x}Pt_x$ films changes accompanied by the structural change from $L1_0$ MnPt to $L1_2$ Mn_3Pt since the peak position of $Mn_{1-x}Pt_x$ (001) gradually shifts to a higher diffraction angle as the Mn sputtering power decreases until it finally arrives at the position of the $L1_0$ MnPt (001) peak. The lattice constants a and c of $Mn_{1-x}Pt_x$ films are extracted from XRD results and shown in the top panel of Figure 2(c) as a function of Mn sputtering power. The a and c change from those of MnPt phase (pink area) to those of Mn_3Pt (green area) with the increased Mn sputtering power. When the Mn sputtering power is less than 48 W, the a value is ~0.28 nm, and when it is higher than 48 W, the a value increases abruptly to ~0.39 nm. The c value shows a moderate increase with increased Mn sputtering power compared to the large change in a. The degree of chemical order, characterized by the ratio of the integral intensity of the (001) peak to that of the (002) peak, also shows an abrupt change near 48 W (middle panel in Figure 2(c)), similar to the variation trend of lattice constants with respect to Mn sputtering power. Figure 2(b) shows Hall resistance versus out-of-plane magnetic field for the $Mn_{1-x}Pt_x$ samples, from which the anomalous Hall conductivity (AHC), defined as $|\sigma_{AHE}| = |\rho_{AHE}| / \rho_{xx}^2$, was extracted. The bottom panel of Figure 2(c) shows AHC as a function of Mn sputtering power. For Mn sputtering power below 48 W, the $Mn_{1-x}Pt_x$ samples are in linear antiferromagnetic MnPt phase, thus showing zero AHC. While, for $Mn_{1-x}Pt_x$ samples with Mn sputtering power over 48 W, a prominent AHC consistent with the emergence of noncollinear antiferromagnetic Mn_3Pt revealed by the XRD results is observed. The noncollinear antiferromagnetism of $L1_2$ Mn_3Pt has been further confirmed for the film sputtered at 56 W by the negligible small magnetization measured by

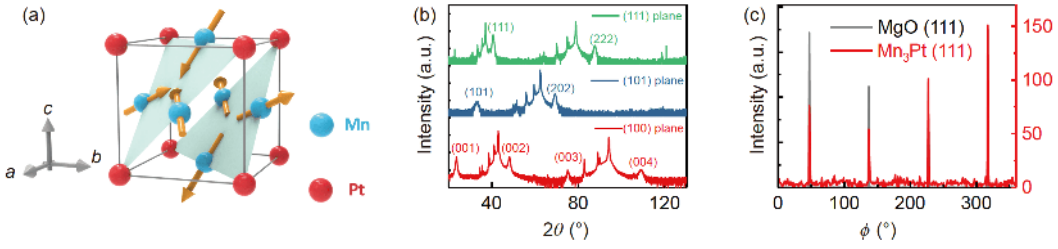

Figure 1 (Color online) (a) Crystal and magnetic structure of cubic Mn_3Pt (blue spheres denote Mn atoms, and red spheres denote Pt atoms, and yellow arrows represent magnetic moments of Mn atoms); (b) out-of-plane θ-2θ XRD spectra of the 25-nm Mn_3Pt at different planes; (c) ϕ scan patterns of the 25-nm Mn_3Pt sample and the MgO substrate.

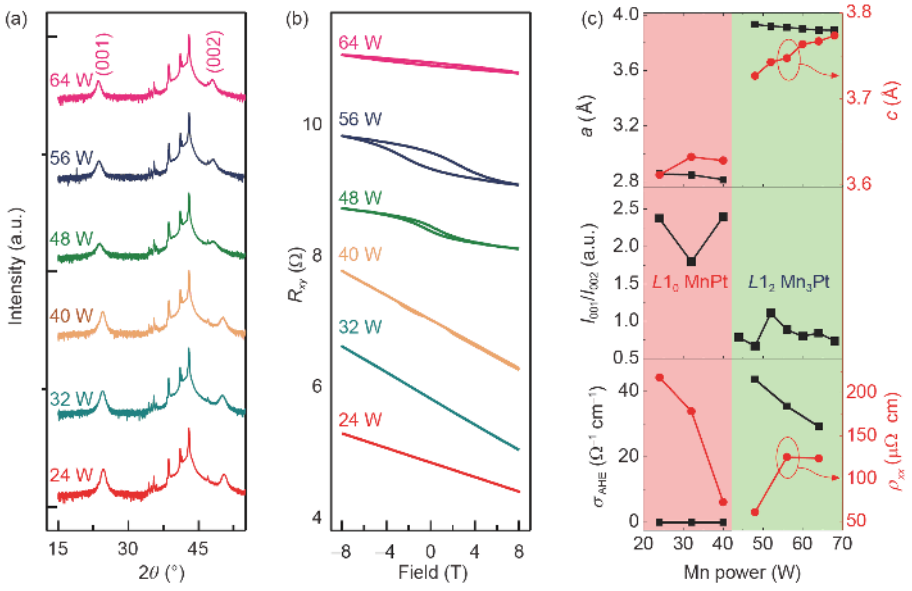

Figure 2 (Color online) (a) Out-of-plane θ-2θ XRD spectra of the $Mn_{1-x}Pt_x$/MgO with different sputtering powers of Mn; (b) Hall resistance versus out-of-plane magnetic field for $Mn_{1-x}Pt_x$ samples; (c) in-plane and out-of-plane lattice constants a and c (top panel), integral intensity ratio of (001) peak to (002) peak (middle panel), σ_{AHE} and ρ_{xx} (bottom panel) as a function of sputtering power.

vibrating sample magnetometer, and the vanishing AHE at elevated temperature above 360 K at which the first-order magnetic phase transition between D phase and F phase happens [13].

After the optimal growth condition has been determined at sputtering powers 56 W for Mn and 30 W for Pt, we then demonstrate the effect of film thickness on the properties of Mn_3Pt. We changed the sputtering time to obtain films with different thicknesses from 6 to 65 nm. XRD measurements show that Mn_3Pt (001) peak shifts to a lower diffractionangle as the film thickness increases, revealing a change in lattice constant c since the lattice constant of the MgO substrate is larger than that of Mn_3Pt. When the film thickness is low, the lattice of Mn_3Pt is severely affected by the substrate; thus, the in-plane lattice of Mn_3Pt is stretched to match that of the substrate, resulting in a relatively large lattice constant a. As the thickness of the film increases, the influence of the substrate weakens, and the lattice of the film is relaxed; a and c, therefore, become close to values of bulk Mn_3Pt. This tuning effect of film thickness on lattice constants is strongly correlated with the strain inside the film. To gain insight into the effect of strain on the magnetic and electrical properties of Mn_3Pt, we measured the AHE loops for the samples. The results are shown in Figure 3(a). A maximal applied magnetic field of 8.5 T is still insufficient to fully saturate the AHE signal of the 44-nm Mn_3Pt film, which is a manifestation of strong magnetic anisotropy of cubic Mn_3Y (Y = Ir or Pt) antiferromagnetic alloy. Therefore, the σ_{AHE} of 44-nm Mn_3Pt film represents a lower bound limit. We found that the coercive force increases with the increase of film thickness, as shown in Figure 3(c), demonstrating a remarkable tuning effect on magnetic properties. Figure 3(b) shows a varying change of AHC with thickness at 300 K. The AHC first increases and then decreases, reaching a maximum value ~98 Ω^{-1} cm^{-1} at 34 nm. This observation is in accordance with the previous study by Liu et al. [13] in which the varying change of AHC with thickness has been discussed with multifold mechanisms. These mechanisms include decreasing surface/bulk ratio with increasing film thickness and different film morphology at different thicknesses. Note that the 34 nm, where the maximal AHC emerges, is also the thickness that allows the strain in Mn_3Pt film to almost fully relax, as can be seen in Figure 4. Therefore, the strain effect together with the afore-mentioned multifold mechanisms proposed by Liu et al. [13] may be responsible for the variation trend of AHC with thickness.

Figure 4(b) shows a and c calculated with XRD results for Mn_3Pt films of different thicknesses to quantitatively demonstrate the change in lattice constants by changing film thickness. The a and c of the Mn_3Pt films vary significantly with thickness when the films are thin, and asymptotically approach the volumetric cubic lattice constant of 0.3833 nm as the films become thicker. The tetragonality factor c/a, closely related to the strain inside films, has also been calculated and manifests a prominent change with d, from 0.968 at 65 nm to 0.937 at 14 nm (Figure 4(c)), indicating a large variation of strain inside the films. To explicitly show the correlation between the strain and film thickness, we quantified the strain inside Mn_3Pt films by carrying out an XRD analysis based on the Scherrer method [35-40]. In this method, the broadening of a diffraction peak is considered being contributed by both the crystallite size and the strain effect. The relation between the full-width at half of the maximum height (FWHM, $\Delta\theta$) and the Bragg angle (θ) of a

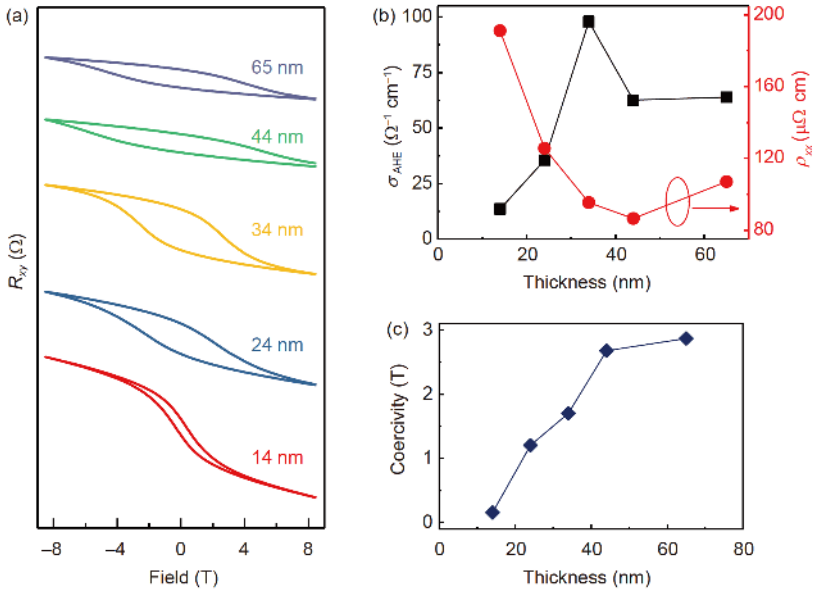

Figure 3 (Color online) (a) AHE loops of Mn_3Pt samples with different thicknesses; (b) σ_{AHE} and ρ_{xx} as a function of thickness at 300 K; (c) coercivity as a function of thickness at 300 K.

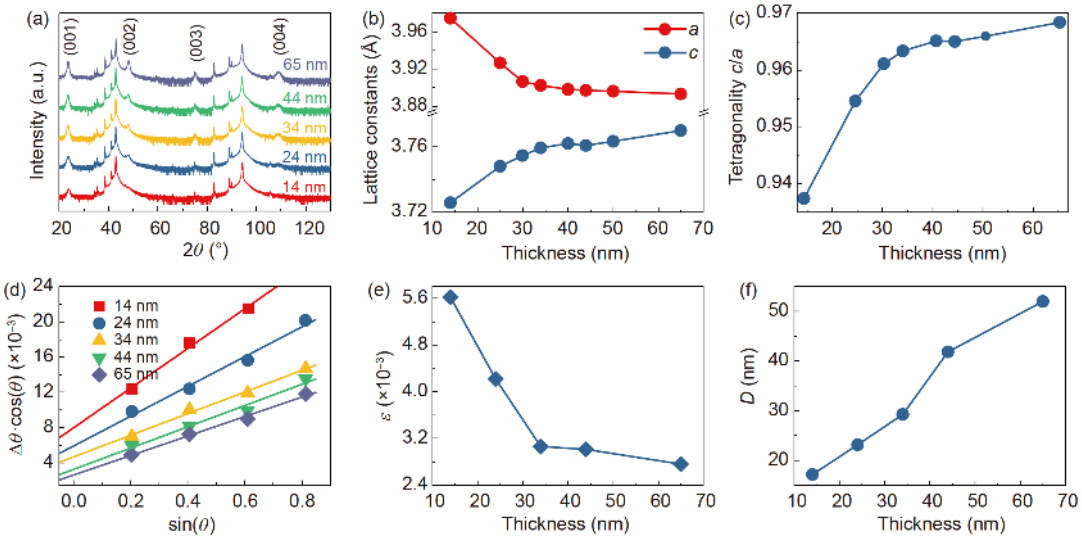

Figure 4 (Color online) (a) Out-of-plane θ-2θ XRD spectra of Mn_3Pt films with different thicknesses; (b) in-plane and out-of-plane lattice constants a and c; (c) tetragonality factor c/a; (d) the extracted $\Delta\theta\cdot\cos\theta$ as a function of $\sin\theta$. The symbols represent experimental data, and the lines are linear fittings. The extracted ε (e) and D (f) versus d.

diffraction peak can be expressed as:

$$\Delta\theta \cdot \cos\theta = \frac{K\lambda}{D} + 4\varepsilon \cdot \sin\theta,$$

where K represents a constant, typically for a cubic symmetry crystal, K is equal to 0.89, λ is the X-ray wavelength, D is the crystallite size, and ε is the strain parameter defined as $\varepsilon = \Delta d / d$.

Using a Gaussian function to fit the diffraction peaks, we obtained $\Delta\theta$ and θ for (00i) (i = 1, 2, 3, 4) peaks. Figure 4(d) shows the values of $\Delta\theta\cdot\cos\theta$ as a function of $\sin\theta$ for Mn_3Pt of different thicknesses. Note that the missing data for (004) peak of 14-nm Mn_3Pt results mainly from a low intensity of this peak since the diffraction volume is quite small. Linear fittings were then applied, and ε and D were derived from the fitted slope and intercept, respectively, and λ = 0.15419 nm was used for the XRD diffractometer using Cu Kα line. Figure 4(e) shows the strain parameter ε as a function of d. The strain first decreases sharply and then gently converges to a constant with increased d, revealing the effectiveness of manipulating strain by varying film thickness. The crystallite size D is also shown in Figure 4(f) and displays a linear increase with d, different from the variation trend of the strain.

4 Conclusion

In summary, we have successfully fabricated epitaxial films of Mn_3Pt on MgO (001) substrates, with noncollinear spin structure. We found that the composition of $Mn_{1-x}Pt_x$ strongly influences AHE as well as the crystal structure. A phase transition from $L1_0$ MnPt to $L1_2$ Mn_3Pt has been observed as Mn concentration in $Mn_{1-x}Pt_x$ increases. Moreover, we manipulated the structural, electrical, and magnetic properties of Mn_3Pt films by changing film thickness. When the film is thin, the lattice constant a is close to that of the substrate and as the film thickness increases, it gradually approaches 0.3833 nm, which is the lattice constant of a bulk Mn_3Pt crystal. The variation of lattice constants with film thickness is attributed to the strain effect. By using the Scherrer method, the strain was quantified, and the relationship between film thickness and the strain has been explicitly revealed. The saturation magnetic field and coercivity field obtained from AHE loops monotonically increase with film thickness, which is also correlated with the strain effect. All the Mn_3Pt films of different thicknesses show large anomalous Hall resistivities. The extracted AHC manifests a varying change with film thickness and reaches the maximum value (98 Ω^{-1} cm^{-1}) at 34 nm, suggesting complex tuning mechanisms in addition to the strain effect. Our work promotes the understanding of AHE in noncollinear antiferromagnetic Mn_3Pt thin film and explores the high-quality Mn_3Pt thin film as a promising candidate for topological antiferromagnetic spintronics [18,41-43].

This work was supported by the National Key R&D Program of China (Grant Nos. 2017YFA0303202, and 2017YFA0305300), the National Natural Science Foundation of China (Grant Nos. 11974260, 11674246, 51501131, 51671147, 11874283, 51801152, and 11774064), the Natural Science Foundation of Shanghai (Grant Nos. 17ZR1443700, and 19ZR1478700), and the Fundamental Research Funds for the Central Universities.

1 E. H. Hall, Philos. **12,** 157 (1881).
2 R. Karplus, and J. M. Luttinger, Phys. Rev. **95**, 1154 (1954).
3 L. Berger, Phys. Rev. B **2**, 4559 (1970).
4 J. Smit, Physica **24**, 39 (1958).

5 N. Nagaosa, J. Sinova, S. Onoda, A. H. MacDonald, and N. P. Ong, Rev. Mod. Phys. **82**, 1539 (2010), arXiv: 0904.4154.
6 P. He, L. Ma, Z. Shi, G. Y. Guo, J. G. Zheng, Y. Xin, and S. M. Zhou, Phys. Rev. Lett. **109**, 066402 (2012), arXiv: 1112.0834.
7 S. J. Xu, Z. Shi, and S. M. Zhou, Phys. Rev. B **98**, 024413 (2018).
8 H. Chen, Q. Niu, and A. H. MacDonald, Phys. Rev. Lett. **112**, 017205 (2014), arXiv: 1309.4041.
9 S. Nakatsuji, N. Kiyohara, and T. Higo, Nature **527**, 212 (2015).
10 A. K. Nayak, J. E. Fischer, Y. Sun, B. Yan, J. Karel, A. C. Komarek, C. Shekhar, N. Kumar, W. Schnelle, J. Kubler, C. Felser, and S. S. P. Parkin, Sci. Adv. **2**, e1501870 (2016), arXiv: 1511.03128.
11 N. Kiyohara, T. Tomita, and S. Nakatsuji, Phys. Rev. Appl. **5**, 064009 (2016), arXiv: 1511.04619.
12 Y. Zhang, Y. Sun, H. Yang, J. Železný, S. P. P. Parkin, C. Felser, and B. Yan, Phys. Rev. B **95**, 075128 (2017), arXiv: 1610.04034.
13 Z. Q. Liu, H. Chen, J. M. Wang, J. H. Liu, K. Wang, Z. X. Feng, H. Yan, X. R. Wang, C. B. Jiang, J. M. D. Coey, and A. H. MacDonald, Nat. Electron. **1**, 172 (2018).
14 Z. H. Liu, Y. J. Zhang, G. D. Liu, B. Ding, E. K. Liu, H. M. Jafri, Z. P. Hou, W. H. Wang, X. Q. Ma, and G. H. Wu, Sci. Rep. **7**, 515 (2017).
15 E. Liu, Y. Sun, N. Kumar, L. Muechler, A. Sun, L. Jiao, S. Y. Yang, D. Liu, A. Liang, Q. Xu, J. Kroder, V. Süß, H. Borrmann, C. Shekhar, Z. Wang, C. Xi, W. Wang, W. Schnelle, S. Wirth, Y. Chen, S. T. B. Goennenwein, and C. Felser, Nat. Phys. **14**, 1125 (2018), arXiv: 1712.06722.
16 D. F. Liu, A. J. Liang, E. K. Liu, Q. N. Xu, Y. W. Li, C. Chen, D. Pei, W. J. Shi, S. K. Mo, P. Dudin, T. Kim, C. Cacho, G. Li, Y. Sun, L. X. Yang, Z. K. Liu, S. S. P. Parkin, C. Felser, and Y. L. Chen, Science **365**, 1282 (2019), arXiv: 1909.09580.
17 N. Morali, R. Batabyal, P. K. Nag, E. Liu, Q. Xu, Y. Sun, B. Yan, C. Felser, N. Avraham, and H. Beidenkopf, Science **365**, 1286 (2019), arXiv: 1903.00509.
18 L. Šmejkal, Y. Mokrousov, B. Yan, and A. H. MacDonald, Nat. Phys. **14**, 242 (2018).
19 N. H. Sung, F. Ronning, J. D. Thompson, and E. D. Bauer, Appl. Phys. Lett. **112**, 132406 (2018), arXiv: 1804.00116.
20 Y. Zhang, J. Železný, Y. Sun, J. van den Brink, and B. Yan, New J. Phys. **20**, 073028 (2018), arXiv: 1704.03917.
21 J. Železný, Y. Zhang, C. Felser, and B. Yan, Phys. Rev. Lett. **119**, 187204 (2017), arXiv: 1702.00295.
22 X. Li, L. Xu, L. Ding, J. Wang, M. Shen, X. Lu, Z. Zhu, and K. Behnia, Phys. Rev. Lett. **119**, 056601 (2017), arXiv: 1612.06128.
23 M. Ikhlas, T. Tomita, T. Koretsune, M. T. Suzuki, D. Nishio-Hamane, R. Arita, Y. Otani, and S. Nakatsuji, Nat. Phys. **13**, 1085 (2017), arXiv: 1710.00062.
24 C. Wuttke, F. Caglieris, S. Sykora, F. Scaravaggi, A. U. B. Wolter, K. Manna, V. Süss, C. Shekhar, C. Felser, B. Büchner, and C. Hess, Phys. Rev. B **100**, 085111 (2019), arXiv: 1902.01647.
25 G. Y. Guo, and T. C. Wang, Phys. Rev. B **96**, 224415 (2017), arXiv: 1708.05933.
26 T. Higo, H. Man, D. B. Gopman, L. Wu, T. Koretsune, O. M. J. van't Erve, Y. P. Kabanov, D. Rees, Y. Li, M. T. Suzuki, S. Patankar, M. Ikhlas, C. L. Chien, R. Arita, R. D. Shull, J. Orenstein, and S. Nakatsuji, Nat. Photon. **12**, 73 (2018), arXiv: 1805.06758.
27 W. Feng, G. Y. Guo, J. Zhou, Y. Yao, and Q. Niu, Phys. Rev. B **92**, 144426 (2015), arXiv: 1509.02865.
28 Y. Kota, H. Tsuchiura, and A. Sakuma, IEEE Trans. Magn. **44**, 3131 (2008), arXiv: 0806.3627.
29 G. Li, Q. Yang, K. Manna, C. Fu, H. Deniz, J. Jena, F. Li, S. Parkin, G. Auffermann, Y. Sun, and C. Felser, Mater. Today Phys. **10**, 100137 (2019).
30 E. Krén, M. Cselik, G. Kádár, and L. Pál, Phys. Lett. A **24,** 198 (1967).
31 E. Krén, G. Kádár, L. Pál, J. Sólyom, P. Szabó, and T. Tarnóczi, Phys. Rev. **171,** 574 (1968).
32 M. Buzzi, R. V. Chopdekar, J. L. Hockel, A. Bur, T. Wu, N. Pilet, P. Warnicke, G. P. Carman, L. J. Heyderman, and F. Nolting, Phys. Rev. Lett. **111**, 027204 (2013).
33 E. Bonera, M. Bollani, D. Chrastina, F. Pezzoli, A. Picco, O. G. Schmidt, and D. Terziotti, J. Appl. Phys. **113**, 164308 (2013).
34 L. Kim, D. Jung, J. Kim, Y. S. Kim, and J. Lee, Appl. Phys. Lett. **82**, 2118 (2003).
35 J. Li, and M. Hitch, Miner. Eng. **86**, 24 (2016).
36 N. Fuson, H. M. Randall, and D. M. Dennison, Phys. Rev. **56**, 982 (1939).
37 A. Monshi, M. R. Foroughi, and M. R. Monshi, WJNSE **02**, 154 (2012).
38 N. Zotov, J. Feydt, and A. Ludwig, Thin Solid Films **517**, 531 (2008).
39 B. F. Ding, Sci. China-Phys. Mech. Astron. **55**, 247 (2012).
40 C. Zhang, G. Pan, J. Luo, W. Li, and D. Chen, Sci. China Ser. G **47**, 1 (2004).
41 T. Jungwirth, J. Sinova, A. Manchon, X. Marti, J. Wunderlich, and C. Felser, Nat. Phys. **14,** 200 (2018).
42 V. Baltz, A. Manchon, M. Tsoi, T. Moriyama, T. Ono, and Y. Tserkovnyak, Rev. Mod. Phys. **90**, 015005 (2018).
43 Z. Feng, H. Yan, and Z. Liu, Adv. Electron. Mater. **5**, 1800466 (2019).